Research Article | Open Access

Soft Science

Shang *et al. Soft Sci.* **2026**, *6*, 63 **DOI:**10.20517/ss.2026.97

Bead-on-string Ag/AgCl heterostructures enable nonpolarizable stretchable dry electrodes for long-term, high-fidelity electrophysiological interfaces

Hengyuan Shang[1,#], Jiangtao Li[1,#], Beibei Shao[1,*], Bo Shi[1], Yuqi Liu[1], Teng Gao[1], Yuxuan Li[1], Yanyun Liu[1], Le Jen Huang[2], Wenzhe Chen[2], Tao Song[1,*], Baoquan Sun[1,3,*]

Keywords:
Stretchable dry electrodes, Ag/AgCl heterostructure, Faradaic interfaces, electrophysiological interfacing, human-machine interfaces

Citation: Shang, H.; Li, J.; Shao, B.; Shi, B.; Liu, Y.; Gao, T.; Li, Y.; Liu, Y.; Huang, L. J.; Chen, W.; Song, T.; Sun, B. Bead-on-string Ag/AgCl heterostructures enable nonpolarizable stretchable dry electrodes for long-term, high-fidelity electrophysiological interfaces. *Soft Sci.* **2026**, *6*, 63. https://dx.doi.org/10.20517/ss.2026.97

Received: 30 Apr 2026
First Decision: 22 May 2026
Revised: 25 May 2026
Accepted: 2 Jun 2026
Published: 9 Jul 2026

Academic Editor: Xinge Yu
Copy Editor: Pei-Yun Wang
Production Editor: Pei-Yun Wang

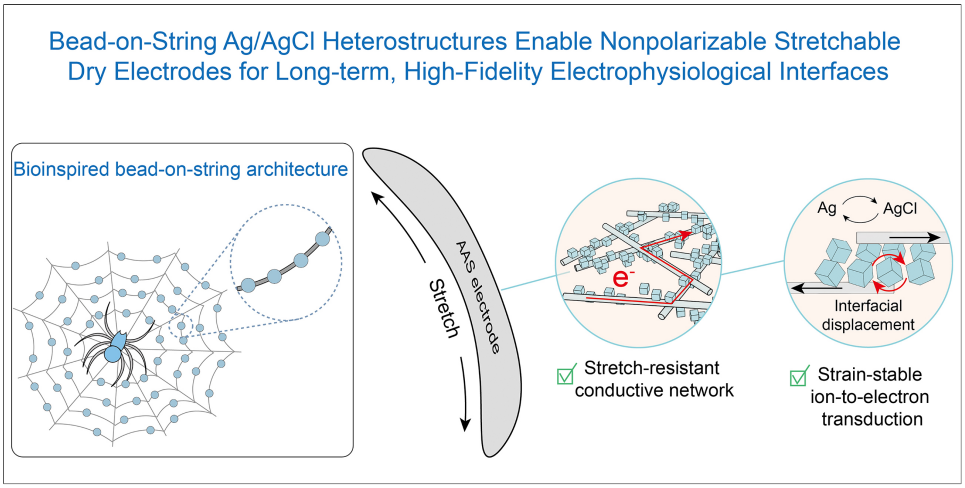

Abstract

Wearable electrophysiological interfaces demand bioelectrodes that combine low-impedance, stable ion-electron transduction with high mechanical deformability, yet these requirements remain fundamentally incompatible in existing systems. Here, we present a nonpolarizable stretchable dry electrode based on a bead-on-string Ag/AgCl heterostructure, in which AgCl nanoparticles (NPs) are selectively assembled along percolated silver nanowire networks embedded within an elastomer matrix. This architecture spatially decouples Faradaic reaction sites from conductive pathways, constructing abundant, mechanically robust Ag/AgCl heterointerfaces for efficient ion-electron transduction while preserving continuous electron transport under large deformation. By systematically tuning the size of AgCl NPs (50-800 nm), the spatial distribution and interfacial length scale of Faradaic domains are optimized to maximize electrochemical performance. The resulting electrode achieves ultralow interfacial impedance (49 kΩ, 10 Hz), stable electrode potentials, and tolerance to severe mechanical deformation (ε > 370%), with minimal degradation over 500 stretch cycles. It enables

[1]State Key Laboratory of Bioinspired Interfacial Materials Science, Institute of Functional Nano & Soft Materials (FUNSOM), Soochow University, Suzhou 215123, Jiangsu, China.
[2]Tripod (Wuxi) Electronic Co., Ltd., Wuxi 214000, Jiangsu, China.
[3]Macau Institute of Materials Science and Engineering, MUST-SUDA Joint Research Center for Advanced Functional Materials, Macau University of Science and Technology, Macau 999078, China.
[#]These authors contributed equally to this work.

[*]**Correspondence to:** Prof. Beibei Shao, Prof. Tao Song, Prof. Baoquan Sun, State Key Laboratory of Bioinspired Interfacial Materials

Science, Institute of Functional Nano & Soft Materials (FUNSOM), Soochow University, Suzhou 215123, Jiangsu, China. E-mail: bbshao@suda.edu.cn; tsong@suda.edu.cn; bqsun@suda.edu.cn

low-noise, high-fidelity signal acquisition in the low-frequency regime, effectively suppressing motion artifacts and maintaining stable operation over 120 days of storage in air. When integrated with a spatiotemporal neural network for electrooculography decoding, the system achieves 98% accuracy in hands-free game control, demonstrating a robust paradigm for next-generation wearable bioelectronics.

INTRODUCTION

Continuous and reliable acquisition of physiological signals is a cornerstone of emerging mobile healthcare systems and human-machine interfaces[1-4]. With the rapid progress of wearable electronics and artificial intelligence[5,6], increasing efforts have been devoted to developing flexible and wearable sensing systems capable of operating stably under dynamic[7], real-world conditions[8] without compromising signal quality. Among these modalities, electrophysiological monitoring places particularly stringent demands on the electrode-skin interface because weak bioelectric signals must be converted into stable electronic outputs with minimal noise and motion-induced fluctuation[9-11]. The simultaneous realization of high-fidelity signal transduction, long-term stability, environmental adaptability, and mechanical compliance remains a critical challenge for next-generation wearable bioelectronics.

In clinical practice, Ag/AgCl electrodes are widely regarded as the gold standard for electrophysiological recording due to their intrinsically non-polarizable Faradaic interfaces[12,13]. These interfaces enable efficient ion-electron transduction through reversible redox reactions, thereby ensuring low interfacial impedance and high signal fidelity[14,15]. However, this favorable interfacial behavior intrinsically relies on the presence of hydrated electrolytes, typically in the form of conductive gels or hydrogels, to maintain sufficient ionic coupling with the skin[14,16,17]. Such gel layers not only require cumbersome skin preparation and may induce skin irritation, but they also suffer from rapid dehydration during prolonged use, leading to severe signal degradation and reduced recording reliability[18,19]. Consequently, these inherent material and operational constraints significantly limit the applicability of conventional Ag/AgCl electrodes in long-term, wearable, and highly dynamic scenarios.

To circumvent the limitations of gel-assisted electrodes, various dry electrodes based on metals[20-24], carbon nanomaterials[25,26], and conductive polymers[27-29] have been extensively explored. However, unlike the non-polarizable Ag/AgCl interface, most dry electrodes rely on capacitive coupling to bridge the skin-electrode interface. Such polarizable interfaces inherently suffer from high contact impedance and severe signal attenuation, particularly in the low-frequency bands critical for electrooculography (EOG) and electrocardiography (ECG), rendering them highly susceptible to motion artifacts[13]. To impart non-polarizable Faradaic properties to dry electrodes, recent efforts have focused on integrating silver nanomaterials into soft elastomers, followed by conventional electrochemical chlorination to form an AgCl layer[30-32]. While this approach improves ion-electron transduction, it introduces a critical structural contradiction. The *in situ* grown AgCl layers are intrinsically brittle and exhibit weak interfacial adhesion with the underlying silver network[33]. Under dynamic stretching or repeated mechanical deformation, these rigid AgCl coatings are prone to severe cracking and delamination[34,35], which disrupts the conductive pathways and drastically increases electrical resistance. Therefore, developing a stretchable dry electrode that simultaneously maintains a robust Faradaic interface, continuous electron transport, and long-term cyclic durability under high strain remains a persistent challenge.

Here, we report a nonpolarizable, intrinsically stretchable dry electrode based on a bead-on-string Ag/AgCl heterostructure, composed of silver nanowires (AgNWs) and pre-synthesized AgCl nanoparticles (NPs) embedded within a poly(styrene-ethylene-butylene-styrene) (SEBS) elastomer matrix, denoted as AgNWs/AgCl/SEBS (AAS), for long-term, high-fidelity electrophysiological interfacing [Figure 1A]. This architecture spatially decouples Faradaic ion-electron transduction domains from conductive pathways, where discretely distributed AgCl NPs provide abundant electrochemical interfaces, while percolated AgNW networks ensure continuous electron transport and mechanical integrity under large deformation. By tuning the size of AgCl NPs (50-800 nm), the spatial distribution and interfacial length scale of Faradaic domains can be precisely regulated, enabling optimized ion-electron transduction capabilities. As a result, the AAS electrode exhibits ultralow skin-electrode impedance (49 kΩ at 10 Hz), stable electrode potentials, and robust electrical performance under large strain (up to 400%), with minimal degradation under repeated deformation. It enables low-noise, high-fidelity signal acquisition in the physiologically relevant low-frequency regime, maintaining stable operation over 120 days and outperforming commercial gel electrodes under dynamic conditions. When integrated with deep-learning (DL)-assisted EOG decoding, the system achieves 98% accuracy in hands-free interactive control. Overall, this work establishes a materials-to-systems paradigm for wearable bioelectronics that require stable ion-electron transduction, mechanical deformability, and long-term operational reliability.

EXPERIMENTAL

Materials

Poly(styrene-ethylene-butylene-styrene) (SEBS, G1651) was purchased from Kraton Co., Ltd. The AgNWs dispersion in ethanol (20 mg/mL, average diameter of 70 nm, length of 20-60 μm) was obtained from XFNANO Co., Ltd. Polyvinylpyrrolidone (PVP, Mw~55000) was purchased from Aladdin. Ag/AgCl gel electrodes were supplied by Cons Medical Equipment Co., Ltd. NIH/3T3 mouse embryonic fibroblasts (1×10^6 cells/T25) were purchased from APExBIO Technology LLC. All other materials, solvents, and reagents were obtained from commercial sources and used without further purification.

Preparation of AgCl NPs

AgCl NPs were synthesized by using a modified reported method[36]. 425 mg of $AgNO_3$ (~50 mM) and 415 mg of PVP (~75 mM) were dissolved in 50 mL of ethylene glycol. After mixing the solution with a magnetic stirrer for 5 min, 6 mL of HCl (~72 mM) was added. The solution was then heated to 150 °C. The reaction was carried out at this temperature for 3-20 min. After the solution cooled to room temperature, 150 mL of deionized (DI) water was added, and the mixture was centrifuged at 7,000 rpm for 10 min. The resulting precipitates were white powder. This rinsing process was repeated three times. The sample was collected after vacuum freeze-drying.

Fabrication of AAS, AgNWs/SEBS, electrochemically chlorinated films

AgCl NPs with different loadings were incorporated into an ethanolic dispersion of AgNWs (45 $mg \cdot mL^{-1}$), yielding inorganic phase dispersions with AgCl concentrations of 15, 30, and 45 $mg \cdot mL^{-1}$. The mixtures were ultrasonicated until a uniform dispersion was obtained. Separately, SEBS powder was dissolved in toluene to afford an organic-phase dispersion at a concentration of 30 $mg \cdot mL^{-1}$. The organic and inorganic dispersions were then mixed at a 5:1 (organic: inorganic) volume ratio and ultrasonicated to obtain a homogeneous precursor solution. Subsequently, 1.2 mL of the precursor solution was cast into a polytetrafluoroethylene (PTFE) mold and covered with aluminum foil. After 24 h of solvent evaporation, a uniform, self-supporting AAS film was obtained. AgNWs/SEBS (AS) films were prepared following the same procedure as for AAS films, except that no AgCl NPs were added to the AgNWs dispersion. Electrochemically chlorinated (EC) films were obtained in a three-electrode configuration using the AS film as the working electrode, with potentiostatic chlorination in 1 M KCl aqueous solution at 0.5 V for 4 min.

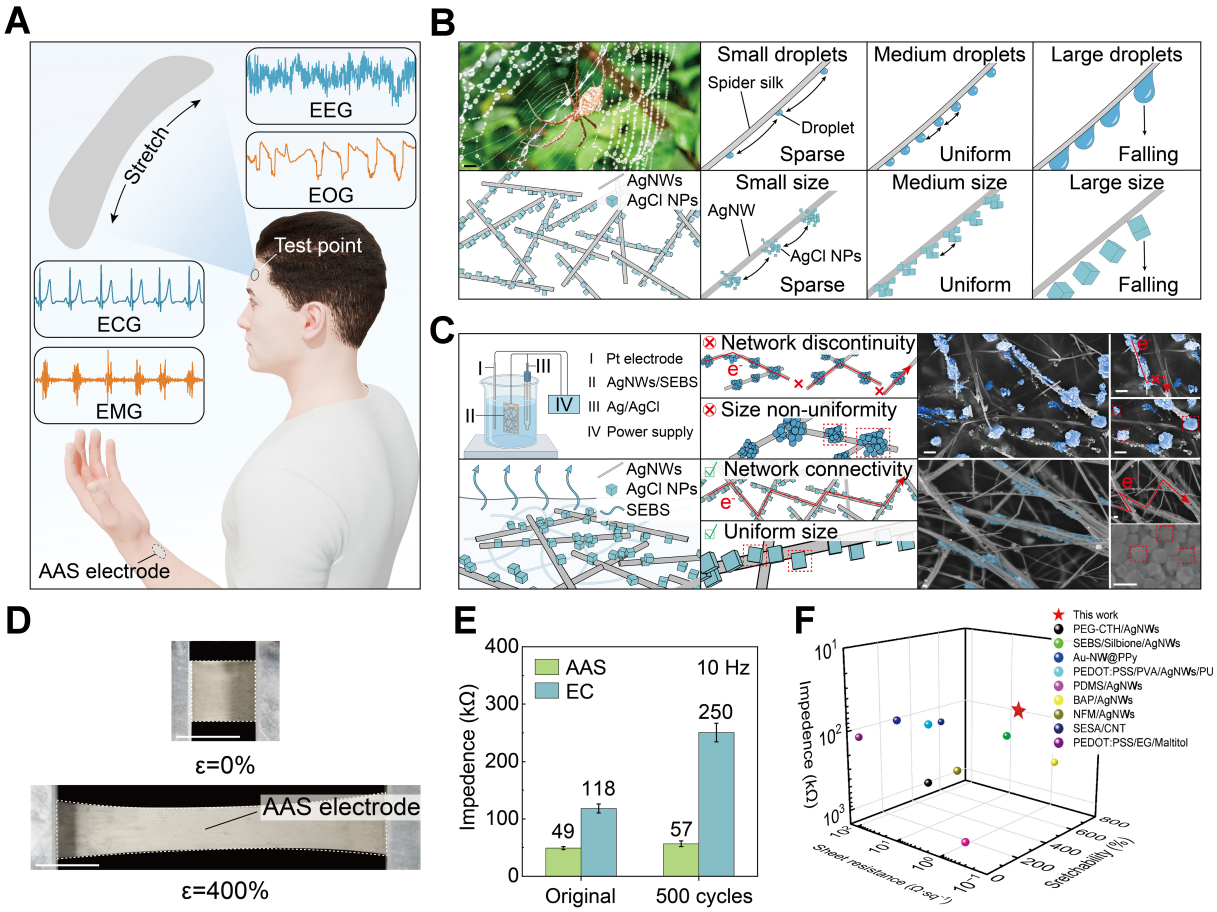

Figure 1. Bioinspired AAS electrode design and performance. (A) Schematic illustration of the AAS electrode for multimodal epidermal electrophysiological monitoring; (B) Bioinspired design concept of bead-on-string architecture inspired by the droplet-on-fiber of spider silk; (C) Structural comparison between electrochemical chlorination (top: EC) and the self-assembly strategy (bottom: AAS), including schematic illustration (left) and corresponding SEM images (right) (scale bars: 500 nm for EC and 100 nm for AAS); (D) Photographs of the AAS electrode under 0% and 400% tensile strain (scale bar: 1 cm); (E) Skin-electrode contact impedance at 10 Hz for AAS and EC electrodes before and after 500 stretching cycles. The error bars indicate the SD obtained from repeated tests (n = 3); (F) Performance comparison of the AAS electrode with recently reported dry electrodes; detailed references are provided in Supplementary Table 1. AAS: AgNWs/AgCl/SEBS [AgNWs: silver nanowires, SEBS: poly(styrene-ethylene-butylene-styrene)]; EC: electrochemically chlorinated; SEM: scanning electron microscope; SD: standard deviation; EEG: electroencephalogram; EOG: electrooculography; ECG: electrocardiography; EMG: electromyogram; AgNWs: silver nanowires; NPs: nanoparticles; SEBS: poly(styrene-ethylene-butylene-styrene); PEG-CTH: polyethylene glycol-tert-Butylcalix arene tetrahydrazide; PEDOT:PSS: poly(3,4-ethylenedioxythiophene)-poly(styrene sulfonic acid); PVA: polyvinyl alcohol; PU: polyurethane; PDMS: polydimethylsiloxane; BAP: bistable adhesive polymer; NFM: nanofibrous membrane; SESA: supramolecular, elastic, self-healing, and adhesive; CNT: carbon-nanotube; EG: ethylene glycol.

Characterization

The morphology of all samples was examined via scanning electron microscope (SEM; G500, Carl Zeiss, USA). The particle size distribution of AgCl NPs was measured using a laser particle size analyzer (Nano ZS90, Malvern Panalytical, UK) with DI water as the solvent. X-ray photoelectron spectroscopy (XPS; AXIS Ultra DLD, UK) was used to determine the chemical composition of all samples. The sheet resistance was measured by using a four-probe resistance tester (ST2258A, Jingge, China).

Measurement of electrical properties

A three-electrode system was employed to study the electrochemical properties of AS, EC, and AAS electrodes using an electrochemical workstation (CHI650E, Chenhua, China). The tested sample (1 cm × 1 cm), platinum plate (1 cm × 1 cm), and Ag/AgCl electrodes were employed as working, counter, and reference electrodes, respectively. Phosphate-buffered saline (PBS) was employed as an electrolyte. For cyclic

voltammetry (CV) measurements, the electrochemical window was set to -1~1 V (*vs.* Ag/AgCl) with a scan rate of 50 $mV \cdot s^{-1}$. Electrochemical impedance spectroscopy (EIS) were obtained with 5 mV amplitude in a frequency range of 10^5-0.1 Hz. For skin-electrode contact impedance testing, electrodes (1.5 cm × 1.5 cm) were attached to the forearm skin, with a spacing of 5 cm between electrodes. The frequency range was 10^5-0.1 Hz.

Measurement of mechanical properties

The tension limit test was performed using a universal testing machine (34TM-50, Instron, USA). Rectangular specimens with a width of 25 mm and a gauge length of 10 mm were stretched at a crosshead speed of 15 $mm \cdot min^{-1}$. Cyclic tensile tests were carried out on a mechanical fatigue system for flexible electronic devices (FlexTest-TM-L, Nanoupe, China), where samples with an initial gauge length of 8 mm were subjected to a tensile loading mode at a stretching speed of 2 $mm \cdot s^{-1}$. In both types of tests, the samples were electrically contacted using copper wires and connected to a source meter (2612A, Keithley, USA) to continuously record variations in resistance during deformation.

Biocompatibility test

The *in vitro* cytotoxicity of AAS was assessed using NIH/3T3. Prior to cell seeding, AAS (1 cm × 1 cm) were rinsed with ethanol and PBS. NIH/3T3 cells were seeded onto the films placed in culture plates and cultured in high-glucose Dulbecco's Modified Eagle's Medium (DMEM) supplemented with 10% fetal bovine serum and 100 $U \cdot mL^{-1}$ penicillin-streptomycin at 37 °C in a humidified atmosphere containing 5% CO_2. For the solvent control group, complete medium containing an equal volume of solvent was added to the cells and incubated under identical conditions. Cell viability after 12 and 24 h of culture was evaluated by confocal laser scanning microscopy. Commercially available NIH/3T3 mouse embryonic fibroblasts were purchased and used. No primary cells, animal experiments, or human-derived biological samples were involved.

Electrophysiological signal recording

For noninvasive electrophysiological monitoring, the flexible electrodes were conformally attached to the skin surface at the target recording sites and connected via lead wires to a wireless biosignal amplifier (NeuSen W, Neuracle, China). The acquired signals were transmitted in real time to a laptop computer over Wi-Fi for data acquisition and subsequent processing. All studies involving human participant was conducted in accordance with the relevant guidelines and regulations. Written informed consent was obtained from the volunteer prior to the experiment. The participant reported healthy neurological, psychological, and dermatological status and participated in tests voluntarily. All electrophysiological experiments involved only non-invasive skin-surface signal monitoring using wearable electrodes and did not include invasive procedures, biological sample collection, or sensitive personal data. Signal-to-noise ratio (SNR) was calculated by root mean square (RMS) as: $SNR = 20\log_{10}\frac{RMS_{\text{signal}}}{RMS_{\text{noise}}}$.

RESULTS AND DISCUSSION

Bioinspired design concept of the AAS electrode

As illustrated in Figure 1B (top), the AAS electrode is rationally designed following a bioinspired bead-on-string architecture, abstracted from the droplet-on-fiber water-collecting behavior of spider silk. In natural spider silk, periodically distributed spindle-knot structures generate gradients in surface energy and Laplace pressure, driving condensed microdroplets to migrate and localize at energetically favorable sites along the fiber. This configuration enables discrete droplets to be organized on a continuous filament, ensuring efficient water collection while preserving structural continuity and mechanical robustness[37]. Notably, this architecture operates within a size-dependent stability window, where droplets remain stably pinned only within an optimal size regime, thereby maintaining an ordered and dynamic distribution along the fiber[38].

Importantly, this bioinspired strategy represents a functional translation rather than a simple morphological analogy. The spider-silk system resolves a fundamental challenge: integrating discrete functional units along a continuous transport pathway without disrupting transport continuity. A similar trade-off exists in stretchable Ag/AgCl electrodes, where high-density electrochemical active sites are required for efficient ion-electron transduction, yet continuous conductive pathways are essential for stable electrical performance. However, random distribution or aggregation of AgCl typically interrupts electron transport and reduces interfacial efficiency.

Guided by this principle, we construct an analogous architecture within a flexible SEBS matrix, as shown in Figure 1B (bottom). The AgNW network serves as a continuous electron-conduction pathway, while AgCl NPs act as discrete Faradaic active sites. When appropriately sized and selectively anchored along the AgNW backbone, the AgCl NPs form a bead-on-string heterostructure that establishes abundant and spatially regulated Ag/AgCl heterointerfaces without compromising network connectivity. This architecture simultaneously maximizes interfacial activity and preserves transport continuity, thereby enhancing ion-electron transduction efficiency and enabling stable electrophysiological interfacing under deformation.

In addition, compared with conventional electrochemical chlorination, our strategy enables the formation of structurally well-defined and spatially regulated Ag/AgCl heterointerfaces while preserving the integrity of the conductive network [Figure 1C]. In electrochemical chlorination, an AS film is immersed in a KCl electrolyte under bias, where Ag is oxidized to Ag^+ and reacts with Cl^- to form AgCl *in situ*. As the reaction proceeds, AgNWs are progressively consumed while sheath AgCl domains grow continuously, yielding an EC film. The generated insulating Ag/AgCl sheath layer disrupts the percolated network, intrinsically inducing structural degradation: oxidative corrosion, which leads to local discontinuity and non-uniform AgCl formation [Supplementary Figure 1]. Moreover, the kinetically governed growth results in randomly distributed, oversized, and electrically insulating AgCl domains, which impede electron transport and compromise mechanical integrity under deformation.

In contrast, our solvent-evaporation-driven self-assembly strategy enables the formation of uniformly distributed AgCl NPs selectively anchored along the AgNW backbone. This bead-on-string architecture establishes abundant and spatially regulated Ag/AgCl heterointerfaces while maintaining continuous electron-conduction pathways, thereby enhancing interfacial electrochemical activity and ensuring structural stability under mechanical deformation.

Such a bioinspired architecture endows the electrode with both mechanical robustness and stable interfacial electrical performance. The AAS electrode sustains large mechanical deformation up to 400% strain [Figure 1D]. To evaluate its dynamic durability, we measured the skin-electrode contact impedance of AAS and EC electrodes before and after 500 stretching cycles at 100% strain [Figure 1E]. The EC electrode exhibits a ~2.1-fold increase in impedance after cyclic deformation, whereas the AAS electrode shows only a minimal ~1.2-fold change, maintaining a stable, low interfacial impedance. When benchmarked against state-of-the-art dry electrodes [Figure 1F and Supplementary Table 1], it exhibits both superior stretchability and stable electrical performance, highlighting its strong potential for next-generation bioelectronic interfaces.

Structure-regulated assembly and interfacial engineering

To construct the targeted AgCl/AgNWs bead-on-string architecture, high-aspect-ratio AgNWs were employed as the conductive scaffold, while AgCl NPs were synthesized via a hydrothermal method[36]. By controlling the reaction time, AgCl NPs with tunable sizes (average edge lengths of 50, 100, 300, and 800 nm) were obtained [Figure 2A and Supplementary Figure 2]. Notably, both AgNWs and AgCl NPs are capped with PVP ligands from their respective synthesis processes, imparting hydrophilic surface characteristics to

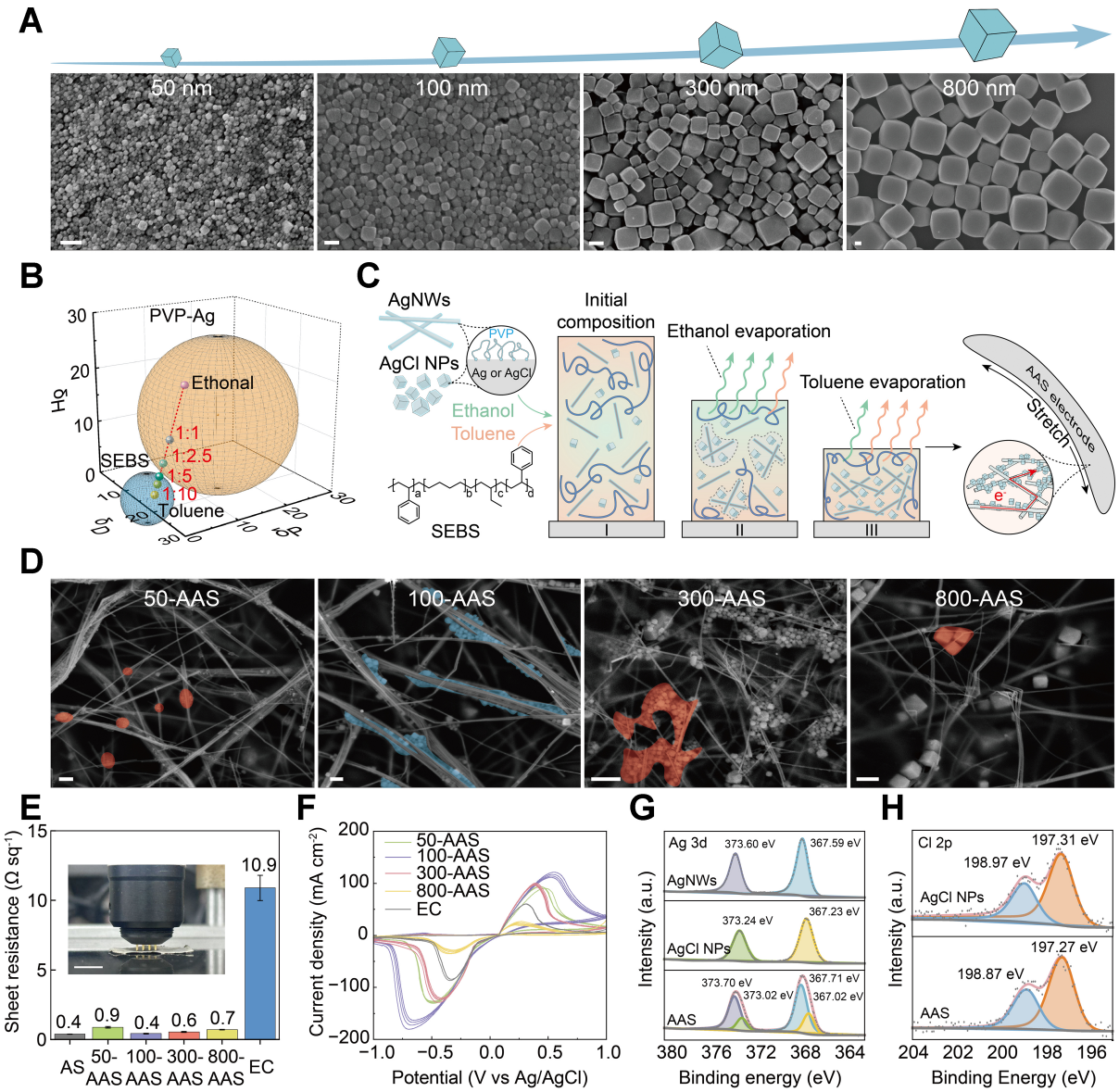

Figure 2. Size-dependent self-assembly of the AgCl/AgNWs heterostructure. (A) SEM images of AgCl NPs with controlled average sizes (50, 100, 300, and 800 nm). Scale bars: 200 nm; (B) HSP space showing SEBS (blue sphere), PVP-Ag (orange sphere), and co-solvents (dots); (C) Schematic of solvent-evaporation-driven self-assembly. AgNWs and AgCl NPs are initially dispersed in ethanol/toluene with dissolved SEBS; preferential ethanol evaporation alters the solvent solubility, driving AgCl NPs to assemble along AgNWs, followed by SEBS solidification to solidify the heterostructure; (D) SEM images of AAS electrodes with AgCl NPs with different sizes (50-AAS, 100-AAS, 300-AAS, and 800-AAS), showing size-dependent assembly. Scale bars: 1 μm; (E) Sheet resistance of AAS electrodes with varying AgCl sizes compared with the EC electrode. The error bars indicate the SD obtained from repeated tests (n = 5); (F) CV curves of AAS electrodes and the EC electrode, highlighting Ag/AgCl interfacial electrochemical activity; (G and H) High-resolution XPS spectra of 100-AAS, AgCl NPs, and AgNWs. AgNWs: Silver nanowires; SEM: scanning electron microscope; NPs: nanoparticles; HSP: Hansen solubility parameter; SEBS: poly(styrene-ethylene-butylene-styrene); PVP: polyvinylpyrrolidone; AAS: AgNWs/AgCl/SEBS [AgNWs: silver nanowires, SEBS: poly(styrene-ethylene-butylene-styrene)]; EC: electrochemically chlorinated; SD: standard deviation; CV: cyclic voltammetry; XPS: X-ray photoelectron spectroscopy.

the nanostructures[39] [Supplementary Figure 3]. When incorporated into a hydrophobic SEBS elastomer matrix, this intrinsic hydrophilicity leads to pronounced thermodynamic incompatibility, resulting in poor dispersion and uncontrolled aggregation [Supplementary Figure 4]. To address this challenge and enable the formation of the desired bead-on-string structure, a rationally designed solvent system was developed. This solvent system ensures homogeneous co-dispersion of the organic and inorganic components at the initial stage and provides a thermodynamically driven assembly pathway during solvent evaporation, thereby guiding the selective anchoring of AgCl NPs along the AgNW backbone.

Therefore, Hansen solubility parameters (HSP) were employed to guide solvent selection. HSP provides a quantitative framework for evaluating intermolecular interactions and predicting miscibility among polymers, solvents, and hybrid fillers[40-42]. Within the HSP framework, the traditional Hildebrand total solubility parameter (δ_T) is decomposed into three types of interaction contributions: dispersion force parameter (δ_D), dipole force parameter (δ_P), and hydrogen bonding force parameter (δ_H), which satisfy the following[43]:

$$\delta_T^2 = \delta_D^2 + \delta_P^2 + \delta_H^2 \quad (1)$$

To quantify the similarity between two substances in HSP space, the Hansen distance R_a is defined[43]:

$$R_a^2 = 4(\delta_{D1} - \delta_{D2})^2 + (\delta_{P1} - \delta_{P2})^2 + (\delta_{H1} - \delta_{H2})^2 \quad (2)$$

Based on this principle, HSPiP software was used to determine the solubility spheres of SEBS and PVP-coated Ag species (denoted as PVP-Ag) [Supplementary Table 2]. The corresponding three-dimensional HSP mapping [Figure 2B] reveals that although the solubility spheres do not fully overlap, they are in close proximity, indicating the feasibility of identifying a solvent system that can simultaneously dissolve SEBS and stabilize PVP-Ag dispersions.

Among various candidates, a binary solvent system of toluene and ethanol was selected for its complementary solvating capabilities and distinct vapor pressures. Toluene effectively dissolves SEBS via nonpolar interactions, whereas ethanol stabilizes PVP-Ag through polar interactions and hydrogen bonding. Notably, the compositional line between toluene and ethanol passes through the overlapping region of the two solubility spheres at an ethanol/toluene volume ratio of approximately 1:5 [Supplementary Table 3], enabling homogeneous co-dispersion of organic and inorganic components.

During solvent evaporation, the dynamic change in solvent composition provides a thermodynamic driving force for the selective assembly of AgCl NPs along the AgNW backbone. This mechanism is further supported by experimental observations, in which uniform precursor solutions are obtained only at the optimized solvent ratio, whereas deviations lead to either poor polymer dissolution or NP aggregation [Supplementary Figures 5 and 6].

The AAS electrode was fabricated by casting a homogeneous precursor solution into a PTFE mold, followed by solvent-evaporation-induced self-assembly [Figure 2C]. During evaporation, the preferential removal of ethanol continuously shifts the solvent composition toward a toluene-rich regime in HSP space, progressively reducing the compatibility with PVP-Ag species. This evolving solvent environment destabilizes the dispersed NPs and nanowires, driving their assembly to minimize interfacial free energy. Consequently, AgCl NPs preferentially aggregate and anchor along the AgNW backbone, forming a bead-on-string architecture. Meanwhile, the increasing concentration of SEBS during solvent evaporation promotes polymer chain entanglement and phase consolidation, which immobilizes the assembled nanostructures. After complete removal of the solvent, a uniform, self-supporting AAS electrode is obtained. The resulting bead-on-string structure extends throughout the film, forming a three-dimensional percolated network with abundant Ag/AgCl heterointerfaces [Supplementary Figure 7].

The assembly of AgCl NPs within the composite is governed by a size-dependent balance between thermodynamic stability and geometric compatibility with the AgNW (with an average diameter of 70 nm) network [Figure 2D]. Accordingly, the samples are denoted as 50-AAS, 100-AAS, 300-AAS, and 800-AAS based on the average edge length of AgCl NPs. Experimentally, distinct assembly behaviors are observed. In

100-AAS and 300-AAS, AgCl NPs preferentially localize near AgNWs, with 100-nm-diameter particles exhibiting the most ordered alignment along the nanowire network, forming a characteristic beads-on-string structure. In contrast, 50-AAS shows severe NP aggregation, while 800-AAS is dominated by isolated particles dispersed in the polymer matrix with minimal association to AgNWs.

This size-dependent morphology can be qualitatively interpreted from a thermodynamic perspective. The dispersion stability is governed by the free energy of mixing (ΔG_{mix})[44]:

$$\Delta G_{mix} = \Delta H_{mix} - T\Delta S_{mix} \tag{3}$$

Where ΔG_{mix}, ΔH_{mix}, and ΔS_{mix} denote the mixing values of Gibbs free energy, the enthalpy, and the entropy. When $\Delta G_{mix} < 0$, the system tends to remain in a uniformly dispersed state. For nanophases (AgNWs and AgCl NPs) and polymer (SEBS), the contribution of ΔS_{mix} is limited because their characteristic dimensions are much larger than those of solvent molecules[45]. As a result, the stability of the system is governed primarily by the enthalpic term. According to Flory-Huggins theory[44], the enthalpy of mixing can be expressed as:

$$\Delta H_{mix} = \chi \phi_1 \phi_2 kT / v_0 \tag{4}$$

Where χ is the interaction parameter, ϕ_1 and ϕ_2 are the volume fractions of the two components, k is the Boltzmann constant, and v_0 is the molecular volume of the solvent. For NPs, it has been suggested that surface energy is more appropriate for predicting their dispersibility rather than cohesive energy[46]. Gårdebjer[47] proposed the following expression:

$$\chi_s = \frac{2v_0}{rkT}(\delta_{\mathrm{T,Nano}} - \delta_{\mathrm{T,Sol}})^2 \tag{5}$$

Where r is the particle radius, $\delta_{\mathrm{T,Nano}}$ and $\delta_{\mathrm{T,sol}}$ are the Hildebrand solubility parameters of the NP and the solvent. This equation indicates that, under the same change in solvent parameters, smaller dispersed NPs exhibit a larger χ_s and consequently a higher ΔH_{mix}.

Based on these considerations, the observed assembly morphology is consistent with a size-dependent self-organization model. Small AgCl NPs (~50 nm) exhibit high interfacial energy, leading to thermodynamic instability and pronounced homo-aggregation. In contrast, excessively large particles (~800 nm) show reduced instability but are geometrically incompatible with the ~70 nm-diameter AgNWs, hindering effective anchoring and resulting in isolated dispersion within the matrix. At intermediate sizes (100-300 nm), the interfacial energy is sufficiently moderated to suppress self-aggregation, while maintaining strong affinity to the AgNW network, enabling ordered bead-on-string assembly. Notably, AgCl NPs with a size of ~100 nm achieve the optimal balance, exhibiting the most uniform distribution and effective interfacial integration. Therefore, an intermediate particle size represents an optimal regime in which the thermodynamic driving force and geometric matching are balanced, enabling the formation of a well-defined AgCl-AgNW heterointerface. This structure establishes continuous electron transport through AgNWs and efficient ion-electron transduction at Ag/AgCl interfaces, forming integrated mixed-conduction pathways throughout the flexible matrix [Supplementary Figure 8].

To correlate structural features with electrical performance, the effects of AgCl NP incorporation on the conductive percolation network and interfacial charge-transfer behavior were evaluated using four-point probe measurements and CV. The results show that incorporating AgCl NPs, regardless of size, preserves the AgNW percolation network [Figure 2E]. The sheet resistances of 50-AAS, 100-AAS, 300-AAS, and 800-AAS

are 0.87, 0.49, 0.55, and 0.71 $\Omega \cdot sq^{-1}$, respectively, remaining comparable to that of the pristine AS film (0.39 $\Omega \cdot sq^{-1}$), indicating minimal disruption to electron transport pathways. In contrast, the EC electrode exhibits a markedly boosted sheet resistance up to 28 times (10.9 $\Omega \cdot sq^{-1}$). This conductivity degradation is attributed to the formation of discontinuous, brittle AgCl domains during electrochemical chlorination, which disrupt inter-nanowire electrical junctions and impede charge transport.

Incorporation of AgCl NPs enhances the interfacial reactivity of the composite films while preserving high electronic conductivity [Figure 2F]. Among all samples, the 100-AAS electrode exhibits the largest CV area and the highest peak current density, indicating enhanced interfacial charge-transfer efficiency[48]. The 50-AAS and 300-AAS electrodes show slightly reduced current responses but retain broad redox features, suggesting effective ion-electron coupling across the Ag/AgCl heterointerfaces. The proposed interaction mechanism between AgCl NPs and AgNWs is illustrated in Supplementary Figure 9, where discrete AgCl domains anchored on the AgNW scaffold form distributed Ag/AgCl interfaces capable of reversible reactions, thereby enabling efficient ion-electron transduction. In contrast, the 800-AAS electrode displays a markedly lower current density, even below that of the EC electrode, reflecting a reduced density of effective Ag/AgCl junctions due to geometric mismatch between oversized AgCl NPs and the AgNW framework. This trend is consistent with skin-electrode impedance measurements [Supplementary Figure 10]. Collectively, these results identify ~100 nm AgCl NPs as optimal for constructing efficient Ag/AgCl heterointerfaces.

The formation of Ag/AgCl heterojunctions was confirmed by XPS analysis of 100-AAS. As shown in Figure 2G, the Ag 3d spectra display two characteristic doublets corresponding to metallic (367.71 and 373.70 eV) and Ag^+ species derived from AgCl (367.02 and 373.02 eV)[49,50]. Compared with the reference spectra of pure components (AgNWs and AgCl NPs), the Ag^0 peaks shift positively (+0.11 eV), while the Ag^+ peaks shift negatively (-0.21 eV), indicating interfacial charge redistribution with electron transfer toward AgCl. Consistently, the Cl 2p spectra exhibit a negative shift relative to pristine AgCl [Figure 2H], further evidencing electronic coupling at Ag/AgCl interfaces. Such interfacial charge coupling facilitates electron transfer across the heterojunction and accelerates ion-exchange kinetics, thereby enabling efficient and reversible redox processes during operation.

Interfacial electrical properties and stability

Efficient physiological signal acquisition requires not only high conductivity but also optimized interfacial properties at the electrode-electrolyte-skin interface, where ionic currents must be effectively transduced into electronic signals[51,52]. This process is governed by interfacial parameters such as charge transfer resistance, capacitive coupling, and electrode polarization, which collectively determine impedance, signal fidelity, and stability within the physiological frequency range (typically 0.1-1,000 Hz).

Owing to the self-assembled and highly coupled AgNWs/AgCl heterointerfaces, the AAS electrode exhibits significantly enhanced interfacial contact properties compared with the AS electrode. To elucidate the role of AgCl content, electrochemical impedance spectroscopy (EIS) was conducted in PBS to simulate physiological conditions. The interface was modeled using an equivalent circuit comprising solution resistance (R_1), double-layer capacitance (C_{dl}), and charge transfer resistance (R_{ct}) [Figure 3A]. As shown in the Nyquist plots [Figure 3B], increasing AgCl content leads to a continuous decrease in the diameter of the high-frequency semicircle, indicating a progressive reduction in R_{ct}. This result demonstrates that incorporating AgCl facilitates interfacial charge transfer and accelerates ion–electron transduction. Notably, as the AgCl loading increases from 25 wt% to 50 wt%, the decrease in R_{ct} gradually approaches saturation, suggesting a limited benefit beyond an optimal loading level.

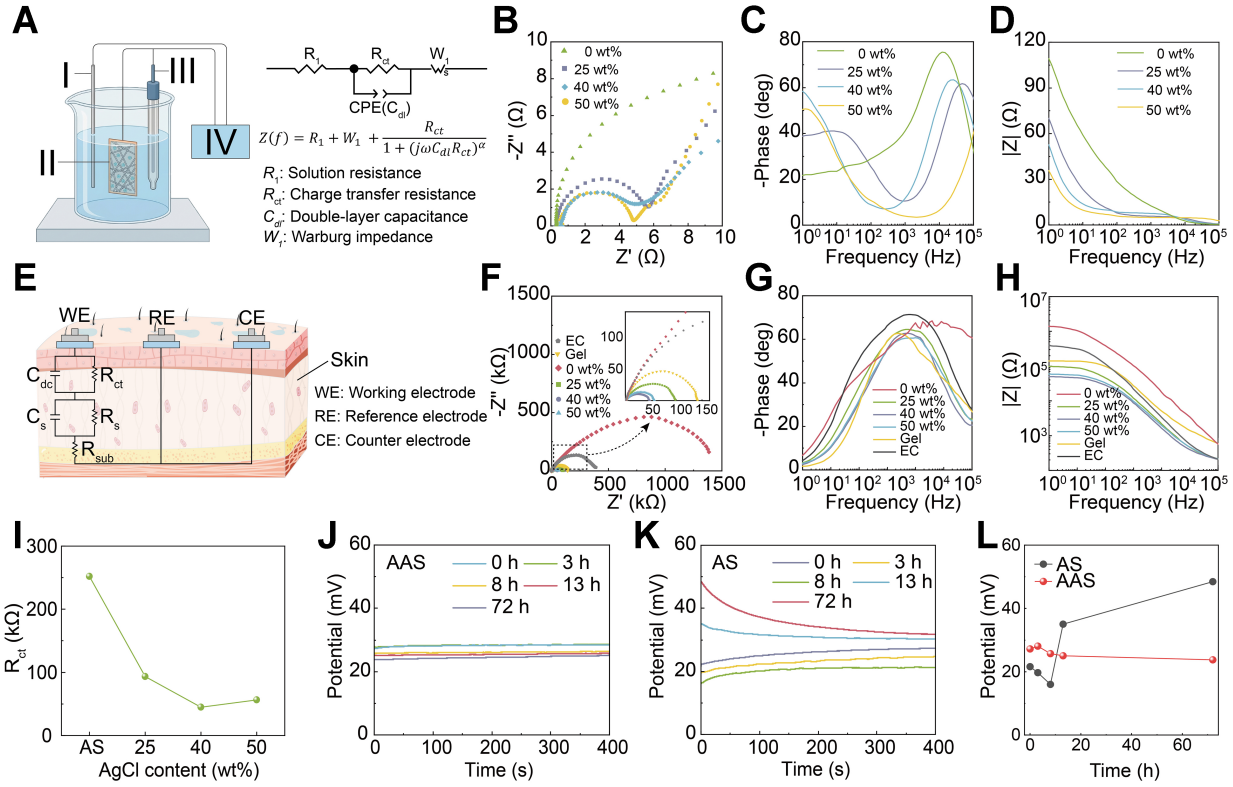

Figure 3. Interfacial electrical properties and stability of the AAS electrode. (A) Schematic illustration of the three-electrode configuration and corresponding equivalent circuit model; (B) Nyquist plots of AS and AAS electrodes with varying AgCl content; Bode plots showing (C) Phase angle and (D) Impedance magnitude as a function of frequency; (E) Schematic illustration of the skin-electrode impedance measurement configuration and the corresponding equivalent circuit model; (F-H) Skin–electrode impedance characteristics: (F) Nyquist plot, and (G and H) Bode plots of phase angle and impedance magnitude; (I) Extracted R_{ct} values obtained from equivalent circuit fitting; (J and K) Open-circuit potential stability of (J) AAS and (K) AS electrodes; (L) Long-term potential drift comparison between AS and AAS electrodes. AAS: AgNWs/AgCl/SEBS [AgNWs: silver nanowires, SEBS: poly(styrene-ethylene-butylene-styrene)]; AS: AgNWs/SEBS; CPE: constant phase element; EC: electrochemically chlorinated.

Bode plots provide further insight into the frequency-dependent interfacial impedance [Figure 3C and D]. With increasing AgCl content, the phase angle across 0.1-1,000 Hz progressively shifts toward 0°, while the impedance magnitude (|Z|) decreases significantly. A phase angle approaching 0° indicates a transition toward resistive-dominated behavior, suggesting effective suppression of capacitive and polarization effects at the electrode-electrolyte interface[53]. This feature is critical for bioelectrical signal acquisition, as a more resistive interface minimizes direct current (DC) offsets and baseline drift[13], thereby improving signal fidelity and reproducibility, particularly for low-frequency recordings. Meanwhile, the reduction in |Z| further confirms a decrease in interfacial resistance, enabling more efficient ion-electron transduction across the interface.

Compared with liquid electrolyte systems, the skin-electrode interface is inherently more complex due to limited and non-uniform electrolyte availability, the high resistance of the stratum corneum, and variable contact conditions[10,13]. To evaluate performance under realistic dry-contact conditions, EIS was conducted using AS, AAS, and EC electrodes on the forearm [Figure 3E]. As shown in the Nyquist plots [Figure 3F], the pristine AS electrode exhibits the highest R_{ct}, indicating inefficient ion exchange and weak electronic coupling at the interface. In contrast, the incorporation of AgCl NPs markedly reduces R_{ct}, demonstrating that the Ag/AgCl heterointerface effectively facilitates ion-electron transduction under skin-contact conditions. Notably, the AAS electrode exhibits impedance characteristics superior to commercial gel electrodes and the EC electrode.

The relatively high impedance of the EC electrode is attributed to the non-uniform distribution of AgCl formed during electrochemical chlorination, which hinders charge transfer. In contrast, the self-assembled Ag/AgCl heterointerfaces in AAS provide uniform and stable ion-electron coupling while maintaining conformal and compliant contact with the skin, thereby suppressing interfacial polarization. With increasing AgCl content (25-40 wt%), the phase angle shifts toward 0° and the impedance magnitude decreases [Figure 3G and H], indicating a more resistive interfacial response and more efficient charge transfer. However, further increasing the AgCl content to 50 wt% results in a slight increase in R_{ct} [Figure 3I and Supplementary Table 4], suggesting that excessive AgCl begins to disrupt the percolated AgNW network.

In addition to low impedance, the AAS electrode exhibits excellent potential stability. As shown in Figure 3J, its open-circuit potential remains nearly constant after three days of immersion in PBS, rapidly reaching equilibrium with minimal fluctuation. In contrast, the AS electrode exhibits pronounced potential drift, particularly during the first 100 s, indicating sluggish ion exchange and an unstable interfacial equilibrium [Figure 3K]. Over an extended operation, the AS electrode further exhibits significant potential fluctuations after 13 h, whereas the AAS electrode maintains a highly stable and reproducible potential [Figure 3L]. These results demonstrate that the incorporation of AgCl establishes a reversible Ag/AgCl redox couple, which stabilizes the interfacial potential by suppressing polarization, thereby reducing drift and improving the reliability of the electrode in practical applications.

Electromechanical stability under strain

An ideal epidermal electrode must retain its electrical performance under mechanical deformation to ensure reliable physiological signal acquisition during body motion. Benefiting from its self-assembled architecture, the AAS electrode exhibits superior mechanical robustness compared with the EC electrode [Figure 4A]. In AAS, AgCl exists as discrete NPs anchored along the AgNW network, allowing interfacial freedom that enables local sliding and relative displacement under strain. This mechanism effectively dissipates stress and preserves network integrity. In contrast, the EC electrode contains rigidly formed AgCl clusters at nanowire junctions, which hinder stress relaxation and induce localized stress concentrations, leading to network fracture under deformation.

Post-deformation SEM images further support this mechanism [Figure 4B]. The 25 wt% AAS film retains an intact, well-defined AgNW network after stretching, with AgCl NPs uniformly distributed along the nanowire surface. In contrast, the EC film exhibits severe network fracture and residual AgCl clusters, indicating substantial structural degradation. Similarly, oversized AgCl NPs exhibit behavior analogous to that of clustered AgCl in EC electrodes, leading to network failure upon stretching [Supplementary Figure 11].

We further examined the AAS electrode with 25 wt% AgCl under tensile deformation [Figure 4C]. SEM observations reveal that upon stretching, the AgNW network deforms, while AgCl NPs anchored to the nanowires undergo relative sliding, thereby dissipating local stress. This behavior is analogous to the bead-on-string configuration in spider silk, which mitigates mechanical damage and preserves network integrity. At the macroscopic level, the film maintains structural integrity up to 400% strain [Figure 4D]. These results indicate that discretely distributed AgCl NPs not only provide interfacial functionality but also enhance mechanical resilience by enabling interfacial sliding under deformation.

Although increasing AgCl content improves interfacial charge transfer and reduces impedance, excessive loading compromises mechanical integrity. To elucidate this trade-off, the mechanical properties of AAS with varying AgCl contents were systematically investigated [Figure 4E]. The pristine AS film exhibits an elongation at break of ~600%. Upon incorporation of AgCl NPs, the Young's modulus increases due to the

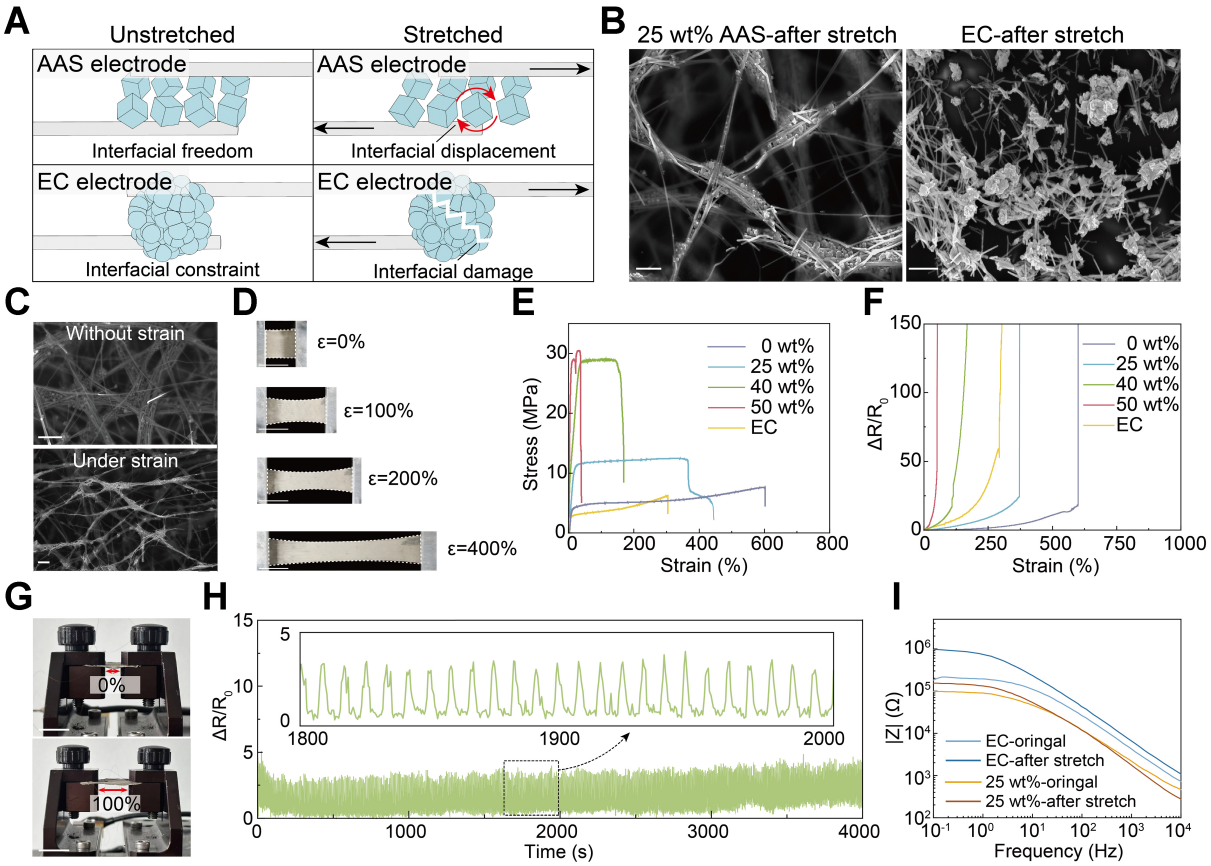

Figure 4. Mechanical and electromechanical performance of the AAS electrode. (A) Schematic illustration of the deformation mechanisms of AAS and EC electrodes under stretching bias; (B) SEM images of the 25 wt% AAS electrode and the EC electrode after stretching. Scale bars: 1 μm; (C) SEM images of the AAS electrode network without strain and under applied strain. Scale bars: 2 μm; (D) Photographs of the electrode under different tensile strains. Scale bars: 1 cm; (E) Stress-strain curves of the AS, AAS electrodes with different filler contents and the EC electrode; (F) Relative resistance change ($\Delta R/R_0$) as a function of strain for the different electrodes; (G) Photographs of the experimental setup for cyclic stretching tests of the AAS electrode at 100% strain. During testing, the electrode was connected to an external source meter via copper wires to record resistance in real time. Scale bars: 1 cm; (H) $\Delta R/R_0$ of AAS electrode during cyclic stretching at 100% strain. The inset shows a magnified view highlighting the periodic changes in resistance of the AAS electrode during cyclic stretching; (I) Impedance spectra of 25 wt% AAS electrode and EC electrode before and after cyclic stretching. AAS: AgNWs/AgCl/SEBS [AgNWs: silver nanowires, SEBS: poly(styrene-ethylene-butylene-styrene)]; EC: electrochemically chlorinated; SEM: scanning electron microscope; AS: AgNWs/SEBS.

rigid filler effect, while extensibility decreases. At 25 wt% loading, the film retains a high elongation at break of ~400%. However, further increasing the AgCl content leads to a sharp increase in stiffness and a dramatic loss of stretchability, with elongation reduced to ~40% at 50 wt%. This behavior is attributed to the disruption of polymer chain entanglement and reduced stress dissipation at high filler concentrations.

Notably, the EC electrode shows a modulus comparable to that of AS but significantly reduced stretchability (~300%), due to irregular AgCl formation that induces stress concentrations under deformation. Strain-dependent resistance measurements further support this trend [Figure 4F]. The 25 wt% AAS electrode maintains stable resistance up to ~370% strain, outperforming the EC electrode (~260%). In contrast, higher AgCl loadings (40-50 wt%) result in fragile conductive networks, leading to a rapid increase in resistance and premature failure beyond ~100% strain. Together with interfacial impedance results, these findings identify 25 wt% AgCl as the optimal composition, achieving a balanced combination of electrical conductivity, interfacial performance, and mechanical compliance.

To evaluate reliability under repetitive deformation, cyclic stretching-relaxation tests were performed at 100% strain for 500 cycles [Figure 4G]. The AAS electrode exhibits excellent fatigue resistance and electrical stability [Figure 4H]. During the initial 1,000 s, the resistance nearly fully recovers after each cycle. With continued cycling, only a slight increase is observed, with the resistance ratio ($\Delta R/R_0$) reaching ~1.1 after 4,000 s (500 cycles), indicating a highly resilient conductive network. In contrast, the EC electrode shows pronounced resistance fluctuations during deformation, with $\Delta R/R_0$ increasing to ~5.7 after 500 cycles [Supplementary Figure 12]. Moreover, AAS electrodes lacking a uniform bioinspired structure display unstable electrical responses under cyclic strain [Supplementary Figure 13], highlighting the importance of the bead-on-string architecture. Under deformation levels more representative of daily skin motion, the AAS electrode also maintained stable electrical performance during repeated stretching cycles [Supplementary Figure 14].

Notably, the Ag/AgCl heterointerfaces in AAS remain functionally active after repeated deformation, as evidenced by only a slight increase in skin-electrode impedance over the 0.1-100 Hz range [Figure 4I]. This result confirms stable ion–electron transduction under dynamic mechanical conditions. Collectively, these results demonstrate that the bioinspired AAS architecture enables robust electromechanical stability by simultaneously preserving the integrity of the conductive network and interfacial functionality under cyclic deformation.

High-fidelity multimodal electrophysiological signal acquisition

To demonstrate its capability for electrophysiological signal acquisition, the AAS electrode was used to record representative signals, including ECG, electromyogram (EMG), electroencephalogram (EEG) and EOG. The low and stable skin-electrode impedance [Supplementary Figure 15], together with favorable biocompatibility [Supplementary Figure 16], enables reliable long-term, conformal signal acquisition. All measurements were performed using a wireless signal amplifier for real-time data acquisition and transmission.

The electrode configuration for ECG acquisition is shown in Supplementary Figure 17. Clinically, ECG analysis primarily relies on the identification of characteristic P, Q, R, S, and T waves complexes to evaluate cardiac electrical activity and rhythm[54]. Therefore, maintaining clear waveform morphology together with low baseline noise and minimal drift is critical for reliable physiological interpretation. The ECG performance was first evaluated under both static and dynamic conditions, as shown in Figure 5A. During motion, relative displacement at the skin-electrode interface induces impedance fluctuations, leading to motion artifacts and waveform distortion. Under these conditions, the AS electrode exhibits severe signal degradation, with indistinguishable ECG features, consistent with its high interfacial impedance and lack of a stable Faradaic interface. The commercial gel electrode also shows noticeable noise during movement. In contrast, the AAS electrode preserves clear, well-resolved P, Q, R, S, and T waveforms, reflecting stable, high-fidelity cardiac signal acquisition even during locomotion. Meanwhile, from a quantitative perspective, the AAS electrode was also able to maintain an excellent SNR during walking [Supplementary Figure 18]. This performance arises from the synergistic coupling of the conformal AgNW network with an anchored Ag/AgCl interface, enabling efficient ion-electron transduction and suppressing interfacial polarization fluctuations. Upon returning to a stationary state, the AAS electrode delivers well-defined ECG signals, whereas the AS and gel electrodes exhibit more pronounced baseline noise. Under static conditions, the signal quality of the AAS electrode is comparable to that of the commercial electrode [Figure 5B].

The long-term signal stability of the electrodes was further evaluated. After 48 h, the commercial gel electrode exhibited an obvious degradation in ECG quality [Supplementary Figure 19], characterized by an unstable baseline and a marked decrease in SNR from 23.9 to 15.4 dB [Figure 5C], primarily due to gel

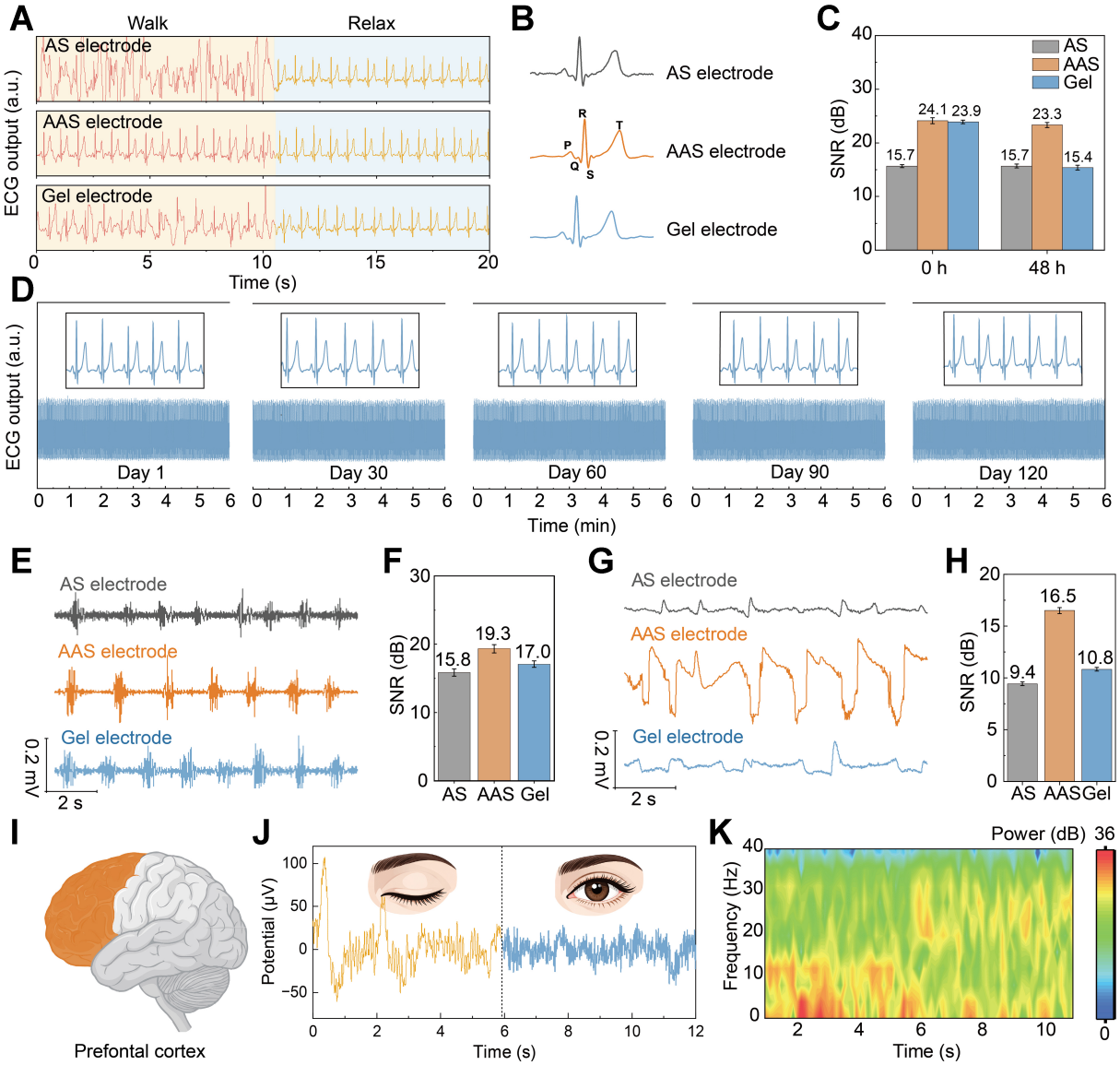

Figure 5. Electrophysiological signal acquisition using the AAS electrode. (A) ECG signals recorded using the AS, AAS, and commercial Ag/AgCl gel electrodes under walking and relaxed conditions; (B) Enlarged ECG waveforms recorded in the relaxed state by different electrodes. Characteristic P, Q, R, S, and T waves are clearly identified from both the AAS electrode and the gel electrode; (C) SNR of ECG signals recorded by the AS, AAS, and gel electrodes at 0 and 48 h. The error bars indicate the SD obtained from repeated tests (n = 5); (D) Long-term storage stability of the AAS electrode was evaluated by ECG recording after storage in air for 1, 30, 60, 90, and 120 days. Insets show enlarged ECG waveforms with well-preserved signal features; (E) EMG signals recorded and (F) SNR values. The error bars indicate the SD obtained from repeated tests (n = 5); (G) EOG signals recorded while looking to the right and (H) SNR values. The error bars indicate the SD obtained from repeated tests (n = 5); (I) The AAS electrode was placed on the forehead to record EEG signals from the prefrontal cortex; (J) EEG signals and (K) corresponding spectrograms recorded using the AAS electrode from a subject with eyes closed (0-6 s) and eyes open with concentration (6-12 s) while awake. AAS: AgNWs/AgCl/SEBS [AgNWs: silver nanowires, SEBS: poly(styrene-ethylene-butylene-styrene)]; ECG: electrocardiography; AS: AgNWs/SEBS; SNR: signal-to-noise ratio; SD: standard deviation; EMG: electromyogram; EOG: electrooculography; EEG: electroencephalogram.

dehydration and the associated deterioration of interfacial ion transport. In contrast, the AAS electrode retained high-quality ECG acquisition after 48 h, with only a negligible change in SNR (23.3 dB). To further assess storage durability, the AAS electrode was tested after prolonged storage in air. As shown in Figure 5D, even after 1, 30, 60, 90, and 120 days, the electrode consistently captured stable ECG signals with well-preserved waveform features. This stability is consistent with the low, stable skin-electrode impedance observed after long-term storage [Supplementary Figure 20], indicating that the AgNW/AgCl

heterostructure remains both electrochemically active and mechanically robust. This further suggests that the AAS electrode can serve as a reusable non-polarizable epidermal electrode without significant performance degradation after repeated use and long-term storage. Overall, these results demonstrate the excellent operational stability and storage durability of the AAS electrode, highlighting its suitability for both immediate use and long-term electrophysiological signal acquisition.

The AAS electrode also demonstrates excellent performance in EMG recording. For forearm EMG measurements, electrodes were attached to the target muscle while the subject performed controlled muscle activation [Supplementary Figure 21]. As shown in Figure 5E, the AAS electrode produces EMG signals with higher amplitude and a more stable baseline than both the AS and commercial gel electrodes. Quantitative analysis further reveals that the AAS electrode achieves the highest SNR of 19.3 dB [Figure 5F], outperforming AS (15.8 dB) and the gel electrode (17.0 dB).

EOG signals originate from the intrinsic dipole of the eyeball, where the cornea is relatively positive, and the retina is relatively negative, forming a stable potential difference[55] [Supplementary Figure 22]. Eye movement alters the dipole orientation, generating potential variations around the orbital region. For EOG acquisition, electrodes were placed at the inner and outer canthi, and the subject was instructed to perform lateral gaze. As a low-frequency (quasi-DC) signal, EOG requires stable, non-polarizable interfaces. The polarizable AS electrode exhibits significant baseline drift, obscuring DC components and capturing only transient peaks [Figure 5G]. In contrast, both the AAS and gel electrodes successfully record step-like eye movement signals, with the AAS electrode delivering a higher average amplitude (~470 μV) and an SNR of 16.5 dB [Figure 5H].

EEG monitoring is a noninvasive technique for recording brain activity, arising from the synchronized electrical activity of neuronal populations that generate weak potential fluctuations on the scalp surface[56,57]. Among characteristic EEG rhythms, the α band (8-13 Hz) is prominent during relaxed states with closed eyes, whereas the β band (14-30 Hz) is associated with alertness and cognitive engagement[58,59]. These features can be effectively captured from the frontal scalp [Figure 5I].

Regarding EEG acquisition, the AAS electrode was placed on the forehead, with reference and ground electrodes positioned on the earlobe [Supplementary Figure 23]. Representative EEG signals were successfully recorded under both eyes-closed and eyes-open conditions [Figure 5J]. To elucidate the spectral characteristics, time-frequency analysis was performed to obtain the power spectral density distribution [Figure 5K]. During the eyes-closed state, the α band (8-13 Hz) exhibited consistently elevated power, whereas upon eye opening, increased activity emerged in the β band (14-30 Hz). Fast Fourier transform (FFT) analysis further revealed a distinct spectral peak within the α band under eyes-closed conditions [Supplementary Figure 24]. These results demonstrate that the AAS electrode can reliably resolve EEG frequency features associated with different cognitive states, highlighting its potential for electrophysiological signal acquisition in brain activity studies and brain-computer interface applications.

Deep learning-enabled human-machine interaction

Building on its high-fidelity and stable EOG signal acquisition, the AAS electrode enables robust, hands-free, and wearable human-machine interaction [Figure 6A]. EOG signals corresponding to upward, leftward, downward, and rightward gaze were recorded and defined as four control commands. The raw signals were preprocessed via filtering, denoising, and segmentation to suppress noise and environmental interference. The processed data were then fed into a DL model based on a hybrid convolutional neural network-bidirectional long short-term memory (CNN-BiLSTM) architecture for the automatic classification of eye-movement directions. The recognized outputs were mapped to directional commands (up, left, down, right)

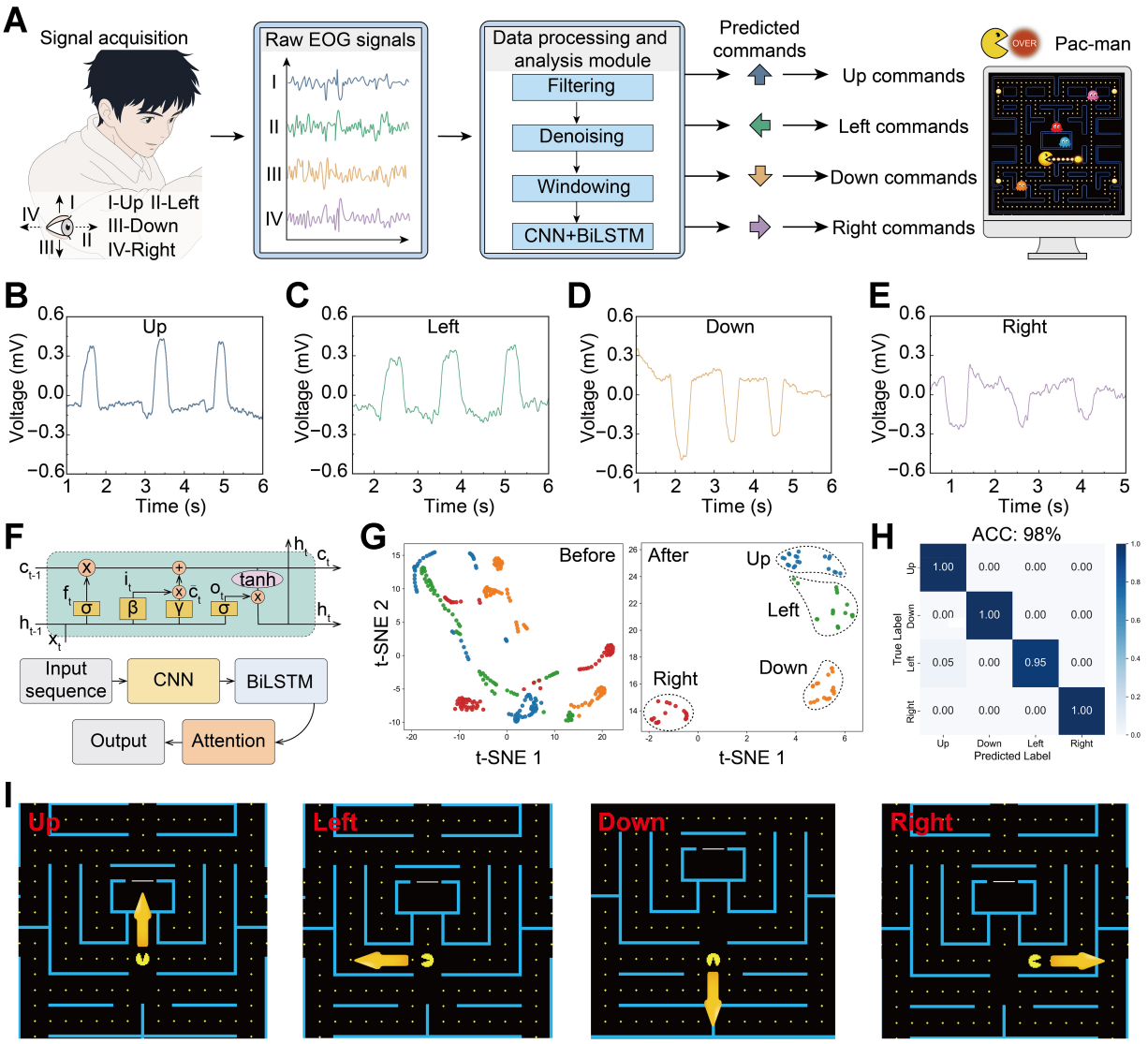

Figure 6. EOG-based human-machine interaction. (A) Schematic illustration of EOG acquisition, signal preprocessing, and deep learning-based command prediction for real-time Pac-Man control; (B-E) Processed EOG signals corresponding to four directional commands (up, left, down, and right); (F) CNN-BiLSTM architecture with an attention mechanism for feature extraction and classification; (G) t-SNE visualization of signal features before and after deep learning-based feature extraction; (H) Normalized confusion matrix for four-class eye-movement recognition; (I) Demonstration of real-time control of a Pac-Man game using EOG signals. EOG: Electrooculography; CNN-BiLSTM: convolutional neural network-bidirectional long short-term memory; t-SNE: t-distributed stochastic neighbor embedding; ACC: accuracy.

to control a Pac-Man game, establishing an EOG-based human–machine interaction system.

Figure 6B-E present representative EOG signals corresponding to the four directional commands. A CNN-BiLSTM architecture with an attention mechanism was employed for feature extraction and classification [Figure 6F]. The CNN module captures local temporal features, while the BiLSTM learns bidirectional temporal dependencies. The attention mechanism further enhances sensitivity to informative signal segments, improving classification performance.

To evaluate feature separability, t-distributed stochastic neighbor embedding (t-SNE) was performed on the features before and after model training [Figure 6G]. In the raw-input state, the signals exhibit partial overlap among classes, indicating limited separability. After feature extraction by the CNN-BiLSTM model, the data

form well-separated clusters, demonstrating that the model effectively learns discriminative representations for different eye-movement directions. The normalized confusion matrix [Figure 6H] demonstrates high classification accuracy, reaching 98%, with minimal interclass confusion. As a result, the subject can reliably control the Pac-Man character in real time through directional eye movements [Figure 6I]. It should be noted that the current model was trained and evaluated on data from a single subject; therefore, the reported accuracy reflects a personalized eye-movement recognition result. This capability highlights the potential of the AAS electrode for intuitive and hands-free human-machine interaction. Such systems may enable applications in assistive communication, wearable electronics, and immersive virtual interfaces.

CONCLUSION

In summary, we have developed a bioinspired, intrinsically stretchable AAS dry electrode featuring a unique bead-on-string architecture. This design elaborately integrates discrete AgCl/AgNWs Faradaic heterointerfaces into a continuous, deformable conductive network. By effectively resolving the trade-off between electrical transduction and mechanical compliance, the electrode achieves an ultralow skin-electrode impedance (49 kΩ at 10 Hz) alongside exceptional electromechanical stability. Remarkably, it can withstand severe mechanical strain of up to 400%, showing only a 1.1-fold increase in resistance after repeated stretching cycles. Consequently, the AAS electrode ensures the high-fidelity acquisition of multimodal electrophysiological signals (ECG, EMG, EOG, and EEG) with robust immunity to motion artifacts. It demonstrates minimal signal degradation during 48 h of continuous operation and maintains outstanding long-term reliability over 120 days. Furthermore, by coupling this hardware with deep learning algorithms, we realized a highly accurate (98%), hands-free human-machine interface based on EOG signal recognition. Ultimately, this materials-to-systems engineering approach establishes a versatile and robust platform for next-generation wearable bioelectronics and intelligent interactive technologies. Further optimization of breathable electrode architectures and patterned interfacial designs is underway to advance the practical applicability of wearable bioelectronic systems.

DECLARATIONS

Authors' contributions

Conceptualization, methodology, funding acquisition, project administration, supervision, writing - review and editing: Shao, B.; Sun, B.

Methodology, funding acquisition, project administration, resources, supervision, writing - review and editing: Song, T.

Data curation, investigation, validation, visualization, methodology, writing - original draft, writing - review and editing: Shang, H.

Data curation, investigation, formal analysis, software, validation, visualization, writing - review and editing: Li, J.

Data curation, formal analysis, software: Shi, B.

Data curation, formal analysis: Liu, Y. (Yuqi Liu)

Investigation: Gao, T.; Li, Y.; Liu, Y. (Yanyun Liu); Huang, L. J.; Chen, W.

Availability of data and materials

The data that support the findings of this study are available from the corresponding author upon reasonable request.

AI and AI-assisted tools statement

Not applicable.

Financial support and sponsorship

This work was supported by the National Natural Science Foundation of China (22408248, 62274116, 62474120), 2025 Independent Research Project of the Jiangsu Provincial Key Laboratory of Carbon-Based Functional Materials and Devices for High-Tech Research (ZZ2506), Macau SAR (0004/2025/RDP), the 111

Program, and the Collaborative Innovation Center of Suzhou Nano Science and Technology.

Conflicts of interest

Huang, L. J. and Chen, W. are affiliated with Tripod (Wuxi) Electronic Co., Ltd., while the other authors have declared that they have no conflicts of interest.

Ethical approval and consent to participate

The study involved only non-invasive placement of wearable devices or skin-surface electrodes on the skin for physiological signal collection and did not involve invasive procedures, biological specimen collection, sensitive personal data, or commercial interests. According to Article 32 of the Measures for the Ethical Review of Life Science and Medical Research Involving Human Subjects (Trial), the study was exempt from formal ethical review. All wearable tests involving human participant was conducted with prior informed consent.

Consent for publication

Informed consent for the use and publication of the images containing personal information included in the Supplementary Materials has been obtained from the individuals involved.

Copyright

Supplementary Materials

Supplementary Materials

REFERENCES

1. Wang, S.; Song, X.; Song, X.; et al. Non-invasive brain-computer interfaces: converging frontiers in neural signal decoding and flexible bioelectronics integration. *Nanomicro. Lett.* **2026**, *18*, 193. DOI PubMed PMC
2. An, X.; Niu, S.; Chen, J.; et al. Flexible electronics in robotics systems: from devices to applications. *SmartBot* **2026**, *2*, e70017. DOI
3. Dong, W.; Chen, X. Research progress of wearable electrochemical biosensors based on metal–organic frameworks (MOFs) for sweat detection. *Adv. Compos. Hybrid. Mater.* **2025**, *8*, 1357. DOI
4. Dong, W.; Chen, X.; Zhai, J.; et al. Structure and application of metal-organic frameworks in wearable electrochemical sweat sensors. *TrAC. Trends. Anal. Chem.* **2026**, *197*, 118738. DOI
5. Zhu, P.; Li, Z.; Pang, J.; He, P.; Zhang, S. Latest developments and trends in electronic skin devices. *Soft. Sci.* **2024**, *4*, 17. DOI
6. Zou, J.; Chen, X.; Song, B.; Cui, Y. Bionic spider web flexible strain sensor based on CF-L and machine learning. *ACS. Appl. Mater. Interfaces.* **2024**, *16*, 23761-70. DOI PubMed
7. Liang, A.; Chen, X. A non-contact porous composite fiber paper-based humidity sensor for wearable breathing and skin humidity monitoring. *J. Mater. Chem. A.* **2024**, *12*, 29081-91. DOI
8. Liang, A.; Dong, W.; Li, X.; Chen, X. A novel dual-mode paper fiber sensor based on laser-induced graphene and porous salt-ion for monitoring humidity and pressure of human. *Chem. Eng. J.* **2024**, *502*, 158184. DOI
9. Buxi, D.; Kim, S.; van Helleputte, N.; et al. Correlation between electrode-tissue impedance and motion artifact in biopotential recordings. *IEEE. Sensors. J.* **2012**, *12*, 3373-83. DOI
10. Kim, K.; Jeong, J. Y.; Shin, J. H.; Kim, T. I. Materials and structures of skin-interfaced electrodes for reducing motion artifacts in neural recording. *Small. Methods.* **2026**, *10*, e01708. DOI PubMed
11. Song, D.; Liu, N. Stable and reliable bio-interfacing electrodes based on conductive hydrogels. *Nat. Electron.* **2024**, *7*, 432-3. DOI
12. Farago, E.; MacIsaac, D.; Suk, M.; Chan, A. D. C. A review of techniques for surface electromyography signal quality analysis. *IEEE. Rev. Biomed. Eng.* **2023**, *16*, 472-86. DOI PubMed
13. Grimnes, S.; Martinsen, ØG. Chapter 7 - Electrodes. In *Bioimpedance and bioelectricity basics*. Elsevier; 2015. pp. 179-254. DOI
14. Polachan, K.; Chatterjee, B.; Weigand, S.; Sen, S. Human body-electrode interfaces for wide-frequency sensing and communication: a review. *Nanomaterials* **2021**, *11*, 2152. DOI PubMed PMC
15. Biesheuvel, P. M.; Porada, S.; Dykstra, J. E. The difference between Faradaic and non-Faradaic electrode processes. *arXiv* **2018**, arXiv:1809.02930. Available online: https://doi.org/10.48550/arXiv.1809.02930. (accessed 2026-07-03).
16. Kang, T. W.; Lee, J.; Kwon, Y.; Lee, Y. J.; Yeo, W. H. Recent progress in the development of flexible wearable electrodes for electrocardiogram monitoring during exercise. *Adv. NanoBiomed. Res.* **2024**, *4*, 2300169. DOI

17. Yang, L.; Gan, L.; Zhang, Z.; et al. Insight into the contact impedance between the electrode and the skin surface for electrophysical recordings. *ACS. Omega.* **2022**, *7*, 13906-12. DOI PubMed PMC
18. Malghan, P. G.; Hota, M. K. A review on ECG filtering techniques for rhythm analysis. *Res. Biomed. Eng.* **2020**, *36*, 171-86. DOI
19. Joutsen, A.; Cömert, A.; Kaappa, E.; et al. ECG signal quality in intermittent long-term dry electrode recordings with controlled motion artifacts. *Sci. Rep.* **2024**, *14*, 8882. DOI PubMed PMC
20. Li, J.; Zhang, S.; Zhong, J.; et al. Laser-induced graphene-assisted patterning and transfer of silver nanowires for ultra-conformal breathable epidermal electrodes in long-term electrophysiological monitoring. *Adv. Funct. Mater.* **2025**, *35*, 2504481. DOI
21. Miyamoto, A.; Lee, S.; Cooray, N. F.; et al. Inflammation-free, gas-permeable, lightweight, stretchable on-skin electronics with nanomeshes. *Nat. Nanotechnol.* **2017**, *12*, 907-13. DOI PubMed
22. Cao, C.; Hou, C.; Wang, X.; et al. Liquid metal-enhanced highly adhesive electrodes for multifunctional epidermal bioelectronics. *Adv. Funct. Mater.* **2024**, *34*, 2403671. DOI
23. Peng, Y.; Song, J.; Zhang, Y.; et al. Permeable, wet-adhesive, and EMI-resistant liquid metal electronic skin for high-fidelity electrophysiological monitoring in sweaty and electromagnetic environments. *Adv. Mater.* **2025**, *37*, e08041. DOI PubMed
24. Ma, J.; Feng, J.; Sa, Z.; et al. High-precision electrohydrodynamic printing of EGaIn-AgNPs biphasic conductive ink for conformal and lightweight bioelectrodes. *Soft. Sci.* **2025**, *5*, 50. DOI
25. Liang, X.; Li, H.; Dou, J.; et al. Stable and biocompatible carbon nanotube ink mediated by silk protein for printed electronics. *Adv. Mater.* **2020**, *32*, e2000165. DOI PubMed
26. Sun, B.; McCay, R. N.; Goswami, S.; et al. Gas-permeable, multifunctional on-skin electronics based on laser-induced porous graphene and sugar-templated elastomer sponges. *Adv. Mater.* **2018**, *30*, e1804327. DOI PubMed
27. Du, X.; Wang, H.; Wang, Y.; et al. An ultra-conductive and patternable 40 nm-thick polymer film for reliable emotion recognition. *Adv. Mater.* **2024**, *36*, e2403411. DOI PubMed
28. Shin, J. H.; Choi, J. Y.; June, K.; Choi, H.; Kim, T. I. Polymeric conductive adhesive-based ultrathin epidermal electrodes for long-term monitoring of electrophysiological signals. *Adv. Mater.* **2024**, *36*, e2313157. DOI PubMed
29. Tan, P.; Wang, H.; Xiao, F.; et al. Solution-processable, soft, self-adhesive, and conductive polymer composites for soft electronics. *Nat. Commun.* **2022**, *13*, 358. DOI PubMed PMC
30. Hu, R.; Yao, B.; Geng, Y.; et al. High-fidelity bioelectrodes with bidirectional ion-electron transduction capability by integrating multiple charge-transfer processes. *Adv. Mater.* **2024**, *36*, e2403111. DOI PubMed
31. Wang, T.; Yao, S.; Shao, L. H.; Zhu, Y. Stretchable Ag/AgCl nanowire dry electrodes for high-quality multimodal bioelectronic sensing. *Sensors* **2024**, *24*, 6670. DOI PubMed PMC
32. Sun, J.; Wang, Q.; Luo, G.; et al. A novel flexible Ag/AgCl quasi-reference electrode based on silver nanowires toward ultracomfortable electrophysiology and sensitive electrochemical glucose detection. *J. Mater. Res. Technol.* **2020**, *9*, 13425-33. DOI
33. Cho, K. R.; Kim, M.; Kim, B.; Shin, G.; Lee, S.; Kim, W. Investigation of the AgCl formation mechanism on the Ag wire surface for the fabrication of a marine low-frequency-electric-field-detection Ag/AgCl sensor electrode. *ACS. Omega.* **2022**, *7*, 25110-21. DOI PubMed PMC
34. Lim, H.; Hillman, N.; Kwon, Y.; Kim, Y.; Choa, Y.; Yeo, W. Ultrathin, long-term stable, solid-state reference electrode enabled by enhanced interfacial adhesion and conformal coating of AgCl. *Sens. Actuators. B. Chem.* **2020**, *309*, 127761. DOI
35. Pargar, F.; Kolev, H.; Koleva, D. A.; van Breugel, K. Microstructure, surface chemistry and electrochemical response of Ag|AgCl sensors in alkaline media. *J. Mater. Sci.* **2018**, *53*, 7527-50. DOI
36. Kim, S.; Chung, H.; Kwon, J.; Yoon, H.; Kim, W. Facile synthesis of silver chloride nanocubes and their derivatives. *Bull. Korean. Chem. Soc.* **2010**, *31*, 2918-22. DOI
37. Zheng, Y.; Bai, H.; Huang, Z.; et al. Directional water collection on wetted spider silk. *Nature* **2010**, *463*, 640-3. DOI PubMed
38. Work, R. W. Dimensions, birefringences, and force-elongation behavior of major and minor ampullate silk fibers from orb-web-spinning spiders - the effects of wetting on these properties. *Text. Res. J.* **1977**, *47*, 650-62. DOI
39. Zhang, P.; Wyman, I.; Hu, J.; et al. Silver nanowires: synthesis technologies, growth mechanism and multifunctional applications. *Mater. Sci. Eng. B.* **2017**, *223*, 1-23. DOI
40. Corzo, D.; Rosas-Villalva, D.; C, A.; et al. High-performing organic electronics using terpene green solvents from renewable feedstocks. *Nat. Energy.* **2023**, *8*, 62-73. DOI
41. Lu, Y.; Jiang, J.; Yoon, S.; et al. High-performance stretchable conductive composite fibers from surface-modified silver nanowires and thermoplastic polyurethane by wet spinning. *ACS. Appl. Mater. Interfaces.* **2018**, *10*, 2093-104. DOI PubMed
42. Stauch, C.; Süß, S.; Luxenhofer, R.; Binks, B. P.; Segets, D.; Mandel, K. Quantifying surface properties of silica particles by combining Hansen parameters and Reichardt's dye indicator data. *Part. Part. Syst. Charact.* **2018**, *35*, 1800328. DOI
43. Hansen, C. M. The universality of the solubility parameter. *Ind. Eng. Chem. Res. Dev.* **1969**, *8*, 2-11. DOI
44. Ravve, A. *Principles of polymer chemistry*, 3rd ed.; Springer New York, 2012. DOI

45. Bergin, S. D.; Nicolosi, V.; Streich, P. V.; et al. Towards solutions of single-walled carbon nanotubes in common solvents. *Adv. Mater.* **2008**, *20*, 1876-81. DOI
46. Süß, S.; Sobisch, T.; Peukert, W.; Lerche, D.; Segets, D. Determination of Hansen parameters for particles: a standardized routine based on analytical centrifugation. *Adv. Powder. Technol.* **2018**, *29*, 1550-61. DOI
47. Gårdebjer, S.; Andersson, M.; Engström, J.; Restorp, P.; Persson, M.; Larsson, A. Using Hansen solubility parameters to predict the dispersion of nano-particles in polymeric films. *Polym. Chem.* **2016**, *7*, 1756-64. DOI
48. Berggren, M.; Malliaras, G. G. How conducting polymer electrodes operate. *Science* **2019**, *364*, 233-4. DOI PubMed
49. Han, L.; Wang, P.; Zhu, C.; Zhai, Y.; Dong, S. Facile solvothermal synthesis of cube-like Ag@AgCl: a highly efficient visible light photocatalyst. *Nanoscale* **2011**, *3*, 2931-5. DOI PubMed
50. Lin, X.; Liu, H.; Guo, B.; Zhang, X. Synthesis of AgCl/Ag/AgCl core-shell microstructures with enhanced photocatalytic activity under sunlight irradiation. *J. Environ. Chem. Eng.* **2016**, *4*, 4021-8. DOI
51. Yuk, H.; Lu, B.; Zhao, X. Hydrogel bioelectronics. *Chem. Soc. Rev.* **2019**, *48*, 1642-67. DOI PubMed
52. Webster, J. G. *Medical instrumentation: application and design*, 4th ed.; John Wiley & Sons, 2009. https://books.google.com/books?id=muRmDwAAQBAJ&lpg=PR5&ots=xXIqtPVfFT&dq=Medical%20instrumentation%3A%20application%20and%20design%2C%20209&lr&hl=zh-CN&pg=PR9#v=onepage&q=Medical%20instrumentation:%20application%20and%20design,%202009&f=false. (accessed 2026-07-03).
53. Romero, M. C.; Méndez-Tovar, M. Impedance analysis for the study of biofilm formation on electrodes: an overview. *J. Mex. Chem. Soc.* **2023**, *67*, 547-65. DOI
54. Kumar, G.; Duggal, B.; Singh, J. P.; Shrivastava, Y. Efficacy of various dry electrode-based ECG sensors: a review. *J. Biomed. Mater. Res. A.* **2025**, *113*, e37845. DOI PubMed
55. Ameri, S. K.; Kim, M.; Kuang, I. A.; et al. Imperceptible electrooculography graphene sensor system for human–robot interface. *npj. 2D. Mater. Appl.* **2018**, *2*, 64. DOI
56. Wang, J.; Wang, T.; Liu, H.; et al. Flexible electrodes for brain-computer interface system. *Adv. Mater.* **2023**, *35*, e2211012. DOI PubMed
57. Li, J.; Chen, G.; Li, G.; Xiao, L.; Jia, R.; Zhang, K. Flexible brain electronic sensors advance wearable brain-computer interface. *NPJ. Biomed. Innov.* **2025**, *2*, 24. DOI PubMed PMC
58. Vourvopoulos, A.; Niforatos, E.; Bermudez, i. Badia. S.; Liarokapis, F. Brain–computer interfacing with interactive systems - case study 2. In: Eslambolchilar, P.; Komninos, A.; Dunlop, M.; editors. *Intelligent computing for interactive system design*. Association for Computing Machinery; 2021. pp. 237-72. DOI
59. Li, Y.; Gu, Y.; Teng, J.; et al. Advancing EEG-based brain-computer interface technology via PEDOT:PSS electrodes. *Matter* **2024**, *7*, 2859-95. DOI